

CHAPTER 9

**Accurate calculations of the high-frequency
impedance matrix for VLSI interconnects and
inductors above a multi-layer substrate:
A VARPRO success story**

Navin Srivastava
Mentor Graphics Corporation
Wilsonville, OR, USA
navin_srivastava@mentor.com

Roberto Suaya
Mentor Graphics Corporation
Grenoble, France
roberto_suaya@mentor.com

Victor Pereyra
CSRC
San Diego State University, CA
vpereyra@yahoo.com

Kaustav Banerjee
Department of Electrical and Computer Engineering
University of California, Santa Barbara, CA 93106, USA
kaustav@ece.ucsb.edu

ABSTRACT. Impedance characterization of Interconnects and intentional Inductors in the broad frequency domain that extends from near DC to 100's of GHz in integrated circuits is full of unachieved goals. Existing computational methods are near the end of their usefulness, since accurate characterization of the Impedance matrix $Z(\omega)$ at high-frequencies with existing methods can only be applied to small structures. We present a computationally inexpensive approach that extends the ability for accurate characterization to problem sizes that are between one and two orders of magnitude larger, opening the door to the validation of high frequency wireless circuits in terms of real time simulation, rather than the less desirable alternative of validation by manufacturing and testing. The starting point in our approach is an integral representation of the Green's function for the magnetic vector potential in classical Electromagnetic theory. The intermediate computation involves a least-square fit to reflection coefficients in terms of linear combinations of complex exponentials, so as to render integrable the coordinate space representation of the Green's function. The end result is an analytical description of derivative quantities, including the matrix elements of the serial Impedance matrix of the interconnect configuration, for all frequencies of interest. We study the problem in two and three dimensions. Among the alternative least square fits, we found that those utilizing VARPRO in the complex domain - an extension of VARPRO created specifically to attack this problem - give the best results. The levels of accuracy (errors less than 3%) and efficiency (better than an order of magnitude lower computational cost than existing methods) have a major impact on nano-electronic circuit design.

Keywords: High-frequency impedance matrix; VLSI interconnects; VLSI inductors; multi-layer substrate; high-frequency wireless circuits; real time simulation; complex exponentials

9.1. Introduction

Very large-scale integrated circuit (VLSI) chips form a complex network of wires (typically Copper) laid out over several metal layers (10 to 14 layers in modern technologies), stacked to a thickness of about 5 to 10 micrometers (μm). The wires lie above the transistors which are themselves implanted on top of a substrate (Silicon) several hundred μm thick. Billions of these wires, called interconnects, provide connectivity between the transistors and ensure circuit functionality at all levels. The lower metal layers are occupied by wires with small cross-sectional area and are used for short connections spanning μm distances between nearby transistors - called "local" interconnects. The delay of these wires is dominated by resistance, R , and capacitance, C (forming R-C diffusion networks) - while dynamic electromagnetic effects are negligible. The top metal layers are used to connect distant components on the chip with "global" interconnects, often spanning mm distances. Since they incur comparatively large delays, these interconnects have larger cross-sections to ensure lower resistance. However, the appreciable inductance (L) makes the impedance (Z) a function of frequency (ω): $Z = R + j\omega L$, where both R and L are functions of frequency beyond a certain threshold. Hence, as the frequency grows, electromagnetic effects become important for computing the propagation delay and noise of these interconnects, and a single complex scalar for each wire segment must be replaced by a complex impedance matrix for an entire chip.

Unprecedented levels of integration in semiconductor technology have enabled complex digital circuits containing billions of transistors to co-exist on the same chip with sensitive analog circuits operating at mm -wavelengths [2]. In the early days

of integrated circuit (IC) technology, the physics of interconnects could be ignored, since their influence on circuit timing (delay) was negligible compared to transistor delay (which itself was orders of magnitude larger than that of today's transistors). Coupling noise due to signals on other wires was also a negligible concern. Since then, while transistor delay has shrunk due to the benefits of progressively decreasing feature sizes (from several micrometers to a few 10s of nanometers), interconnects have come to play a much more significant role in determining overall circuit timing and functionality [15]. Today, with 20 *nm* feature sizes on a chip, the propagation time of signals over 1 *mm* distances is significantly slower than the transition time of a logical switch [2], while noise propagation among nearby wires can lead to chip failures. As a result, the physics of signal propagation on interconnects in a complex semiconductor chip has become a subject of deep concern. The most important application domains sensitive to signal propagation on interconnects are those of inductor design with applications in radio receivers and communications chips, as well as timing-critical signal lines in high-performance digital microprocessors. In the frequency domain, the region of interest extends from near zero up to hundreds of GHz for both analog wireless and high-performance microprocessor design.¹

The physics of signal propagation on wires falls within the combined domain of electromagnetism and the constitutive equations of electron propagation on metals (Ohm's law in the frequency domain) and dielectrics (wave propagation in lossy media). The fundamental equations are well understood. The complexity and associated computational cost, on the other hand, is prohibitively large for chip-level solutions due to three underlying reasons: (i) the large number of wires and inductors, (ii) the multi-layered nature of both the dielectric media and the substrate profile where these phenomena take place, and (iii) the interval of wavelengths where these phenomena are to be accounted for includes (at the lower end) wavelengths of the same order as the longitudinal dimensions of the wires. This is the domain in which most approximations (short or long wave) fail. In this frequency domain, several physical phenomena are manifest - the conductor skin effect, proximity effects between conductors, and substrate eddy current effects. Together they impact the current distribution and, through Ohm's law, the macroscopic Impedance and Admittance matrices that are used to represent the interconnect.

In the regime where signal propagation wavelengths are larger than chip dimensions, electromagnetic effects have no measurable consequences and simple treatments of interconnect as distributed resistance-capacitance (R-C) networks suffice. There is a body of work [11], [22], [18], that discusses appropriate numerical methods for wavelengths between 1 – 10*cm* where currents are uniform inside the wires. For wavelengths between 1 – 10*mm*, currents cease to be uniform due to a limited penetration of the magnetic field \vec{B} inside the conductors. Under these conditions, the computational expense of these numerical methods increases rapidly with decreasing wavelength, and new approaches have been developed [9], eventually leading to efficient analytical methods [21]. As the wavelengths become smaller than

¹ The maximum frequency of signal propagation on interconnects is much larger than the more familiar "clock" frequency. It is inversely proportional to the rise time of the signal driven by the fastest transistor feeding the interconnect.

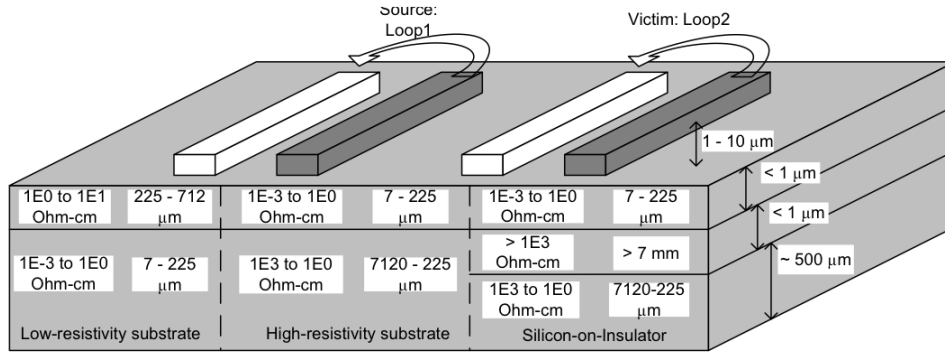


FIGURE 9.1.1. Schematic showing interconnect current loops over a layered substrate. Three typical substrate profiles in VLSI are shown with the range of resistivity ($\rho = \frac{1}{\sigma}$ Ohm-cm) values, and the corresponding skin depth - the depth of penetration of electromagnetic fields in the medium, given by $\delta = \sqrt{2/(\omega\mu\sigma)}$ - at 50 GHz.

2mm, the Silicon substrate media presents a path for current circulation that cannot be ignored, further exacerbating the challenge of computing the Impedance and Admittance matrices.

In this work, we discuss the consequences of including the substrate effects in the computation of the impedance matrix while still maintaining analytical solutions [25], [23]. The overall result is a uniform treatment from infinite wavelengths down to wavelengths comparable to the longitudinal dimensions of the interconnects. Due to lack of space, we give only a brief background of the physics in our approach, concentrating instead on the approximations to the Green's function formulation for the Magnetic Vector Potential of the magnetic field, in the presence of a multi-layered substrate. In particular, we show that the ability to use a linear combination of complex exponentials to approximate the reflection coefficients appearing in the spectral representation of the Green's function, leads to analytical expressions for the Green's function in coordinate space. Furthermore, we find that subsequent manipulations involving multi-dimensional (four to six) integrals involving the Green's function to extract the Impedance matrices can also be carried out analytically by using the initial approximation. The resulting Impedance matrices have less than 3% error when the complex exponential approximations are obtained using a complex extension of VARPRO (discussed in Chapter 1). Alternative methods do not lead to the same level of accuracy [25], especially for 3D problems [23]. Specialized 3D full electromagnetic field solvers [1] at the same level of accuracy are computationally expensive and do not permit us to scale the problem space beyond very simple structures. The computability and accuracy of our approximation method is made possible in part by the presence of accurate and smooth fits with VARPRO using complex coefficients.

9.2. Green's function computations

In digital integrated circuits, the interconnects are laid out along Cartesian directions ($\hat{x} - \hat{y}$) on the different metal layers. Each metal layer has interconnects running along one direction only (\hat{x} or \hat{y}), with those on adjacent layers being orthogonal to each other (called Manhattan geometry), and vertical links (called vias) connecting them where needed. The number of wires in a modern high-performance microprocessor chip can be as large as 10^{10} , and the space of possible routes in three dimensions for these wires is quite large. It is necessary to identify the much smaller set of wires whose propagation delay and voltage noise can impair the functionality of the chip as a whole, and to do so we accurately compute their impedance parameters. On-chip interconnects in analog circuits do not always conform to Manhattan geometry and may have arbitrary orientation. This complicates the electromagnetic interaction at the lowest level, since it is computationally a much simpler problem to compute the capacitance and inductance of wires constrained along Cartesian directions. Moreover, while the number of circuit components (and hence, the number of wires) in analog designs is several orders of magnitude smaller than that in digital designs, the desired level of accuracy for impedance calculation of these wires is an order of magnitude higher. As much as 10% error in the electromagnetic parameters for critical wires may be acceptable in digital applications, while an order of magnitude better precision is demanded for passive inductors and transformers used in wireless analog designs. Increasingly common "mixed-signal" designs - digital circuits with several analog components included on the same chip - represent the most demanding scenario in terms of computational complexity, combining the large size of digital designs with the need for high accuracy in sensitive analog circuits.

We are interested in divergence free electromagnetic currents in the interconnects, such that:

$$\begin{aligned} \nabla \cdot \vec{J} &= 0 && \text{in the conductor volume} \\ \nabla \cdot \vec{J} &= -j\omega q && \text{on each conductor surface} \end{aligned} \quad (9.1)$$

where J is the current density, $\omega = 2\pi f$ is the signal frequency, and q is the charge density on the conductor surface. The relaxation time (τ) for free charges in Copper [6]:

$$\tau = \epsilon/\sigma = O(10^{-18})\text{seconds}, \quad (9.2)$$

is much smaller than the time constants at the maximum signal frequency $f < 200GHz$, allowing us to neglect the effect of displacement currents inside the conductors.

A signal wire segment carrying rectilinear one-dimensional currents, and one or more nearby parallel power/ground wire segments capacitively coupled to the signal wire, together form our basic representation for a closed current loop. The power/ground wire segments share the current flowing through the signal wire among themselves in a direction opposite to that of the signal current, and are referred to as carriers of the return current, or simply return paths. In terms of the electric circuit for the closed current loop, the signal wire is represented by an impedance in series with the parallel combination of the impedances of all its return paths. The capacitors that couple the return paths to the signal wire can be computed separately with a field solver from the geometric data representing the wires. The collection of an interconnect and its return paths is partitioned along

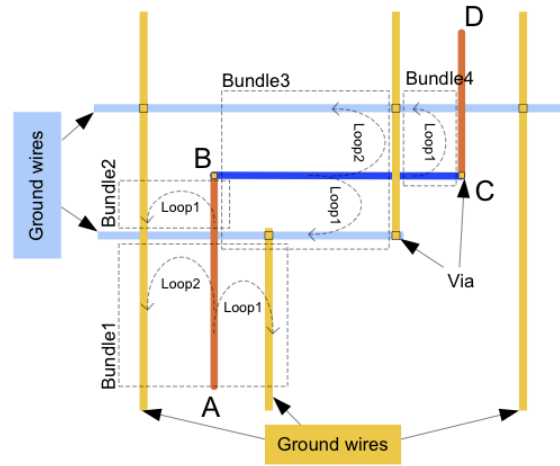


FIGURE 9.2.1. A VLSI interconnect with linear segments AB - BC - CD flanked by ground wires which offer return paths. Segmentation of the interconnect configuration into *bundles*, along with the constituent *loops*, are shown with dashed boxes and curves, respectively.

their length to form "bundles" [11] such that all wires in a bundle have the same length. Thus, per-unit-length quantities can be computed for each bundle using a 2D approach. Fig. 9.2.1 illustrates the partition of an interconnect configuration into bundles, and the constituent current loops.

9.2.1. Two-dimensional (2D) interconnect. The previous paragraph described the physical picture of the "current loops" for interconnect impedance computation in digital chips. An alternative to the "loop impedance" computed using this approach [11] is the "partial impedance" computed using the Partial Elements Equivalent Circuit (PEEC) approach [22]. Under PEEC, every segment of wire is considered independent from all other wire segments, and signal and return paths are not distinguished while building the impedance matrix. The closed path of physical currents is imposed a posteriori during circuit simulation, via the application of Kirchhoff's laws, making all possible paths available when solving the large linear system. Since the long distance behavior of the partial impedance decreases logarithmically with the separation between wire segments, as opposed to the inverse power law behavior of the physical loop impedance [11], the impedance matrix in the PEEC is dense and not diagonally dominant. In the loop impedance formalism, mutual impedances between interconnect loops are appreciable only for separations smaller than ten times their transverse dimensions [11] resulting in diagonally dominant sparse impedance matrices. In terms of interconnect length, inductance effects are important when the time of flight for a signal along the interconnect length is comparable to the transition time of the logic driving the signal [10]. This requirement translates into wire lengths longer than $100\mu m$ for on-chip interconnects in the nanometer regime. Since the interconnect widths are seldom larger than a few microns, and the transverse separations where mutual impedance is important are equally bounded, it follows that for a substantial number of global

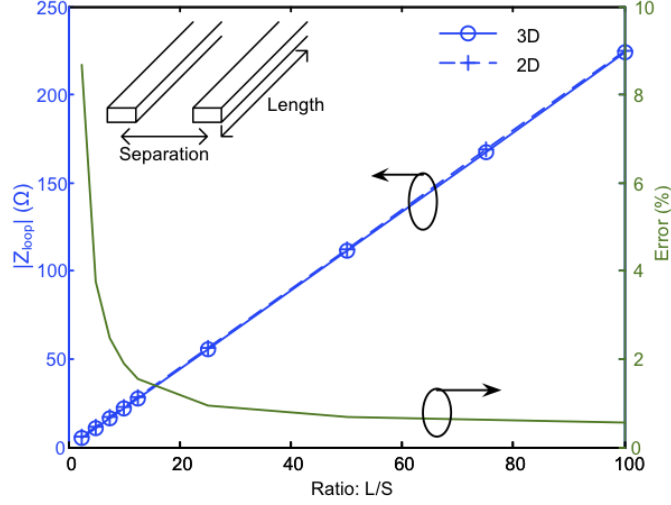


FIGURE 9.2.2. Comparison of 2D loop impedance computation with 3D computation (left y-axis) as a function of the ratio of conductor lengths to transverse separation (L/S), in presence of a 3-layer substrate, at 100 GHz. Error (%) due to the 2D approximation is shown on the right y-axis.

on-chip interconnects a two-dimensional (2D) analysis of electromagnetic effects will suffice.

Fig. 9.2.2 shows that the error in loop impedance when using the 2D approximation is quite small when the conductor lengths exceed 10 times the transverse separations between them.

A physically equivalent representation of a planar current loop is a magnetic dipole [17], as shown in Fig. 9.2.3. Since on-chip conductors are confined to discrete metal layers in the x - y plane (neglecting vias which have small dimensions), the current loops they form are planar, although they may have arbitrary orientations (ϕ). For a planar loop carrying current I , its magnetic dipole moment \vec{p} is perpendicular to the plane containing the loop, and its magnitude is given by [17]:

$$|\vec{p}| = I \times LoopArea \tag{9.3}$$

Rotational symmetry allows us to choose the y -axis along the length of the wires forming the current loop, and this dimension is omitted in the 2D treatment. \vec{p} has horizontal and vertical components:

$$\vec{p} = p_x \hat{x} + p_z \hat{z} = |\vec{p}| [\sin(\phi) \hat{x} + \cos(\phi) \hat{z}] \tag{9.4}$$

9.2.2. Integral representation of the 2D Green's function. Consider two opposite currents $I\hat{y}$ and $-I\hat{y}$, centered at (x', z') and separated by an infinitesimal distance a , lying above a multi-layered substrate. The two currents constitute a \hat{z} -directed 2D magnetic dipole.

In the region R_0 above the substrate, the corresponding \hat{y} -directed vector potential Green's function G_{ver}^{d, R_0} for a \hat{z} -directed unitary magnetic dipole source, with

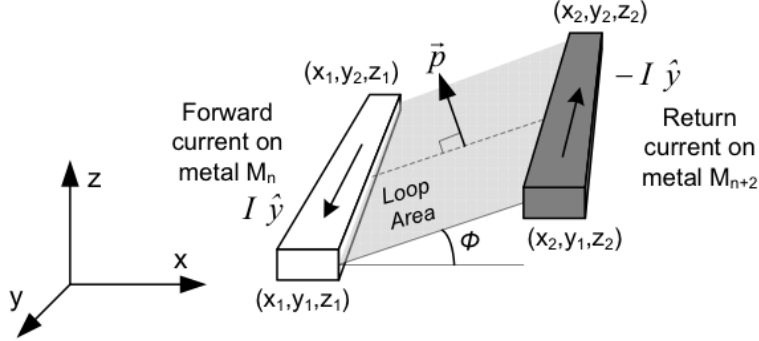


FIGURE 9.2.3. Current loop formed by two parallel current filaments carrying current in opposite directions constitutes a planar magnetic dipole source.

$I \rightarrow \infty$ and $a \rightarrow 0$ such that the dipole moment $|\vec{p}| = \frac{\mu}{2\pi}(Ia) = 1$, satisfies:

$$\begin{aligned} \nabla^2 G_{ver}^{d,R_0}(x, z, x', z') = \\ \lim_{a \rightarrow 0} \frac{-2\pi}{a} \left[\delta(x - x' + \frac{a}{2})\delta(z - z') - \delta(x - x' - \frac{a}{2})\delta(z - z') \right]; z, z' > 0 \end{aligned} \quad (9.5)$$

Since there are no sources inside the substrate, the Green's function in region R_i satisfies:

$$(\nabla^2 - \gamma_i^2)G^{R_i}(x, z) = 0; z < 0 \quad (9.6)$$

where $\gamma_i^2 = j\omega\mu(\sigma_i + j\omega\epsilon_i)$ for the i^{th} substrate layer.

Using the Fourier transform in x and continuity of the magnetic field at the interface boundaries between different regions, we obtain for an N -layer substrate:

$$\begin{aligned} G_{ver}^{d,R_0}(x, z, x', z') \\ = - \int_0^\infty \left(e^{-k_x|z-z'|} - \chi_N(k_x)e^{-k_x(z+z')} \right) \sin(k_x(x-x')) dk_x; \quad (9.7) \\ k_z = jk_x \end{aligned}$$

The above dipole Green's function expression is a sum of two terms: a *primary* term corresponding to the magnetic dipole in free space, and a *secondary* term which is nearly identical in form (except for the coefficient χ_N) arising due to reflections at the interfaces in the substrate. While the expressions for the primary and secondary field terms above may vary depending on the source (such as electric or magnetic dipoles), the coefficient χ_N always remains unaltered [7], [16], [24]. The Green's function for a horizontal magnetic dipole under the same boundary conditions is:

$$\begin{aligned} G_{hor}^{d,R_0}(x, z, x', z') \\ = \begin{cases} - \int_0^\infty \left(e^{-k_x|z-z'|} + \chi_N(k_x)e^{-k_x(z+z')} \right) \cos(k_x(x-x')) dk_x, & z > z' \\ - \int_0^\infty \left(-e^{-k_x|z-z'|} + \chi_N(k_x)e^{-k_x(z+z')} \right) \cos(k_x(x-x')) dk_x, & z < z' \end{cases} \end{aligned} \quad (9.8)$$

In general, $\chi_N(k_x)$, the term characterizing the substrate contribution for an N -layer substrate, can be cast into the form:

$$\chi_N(k_x) = \frac{Q_N(k_x) - k_x}{Q_N(k_x) + k_x} \quad (9.9)$$

where the terms $Q_N(k_x)$ depend only on the substrate properties: conductivity σ , permittivity ϵ , permeability μ of each substrate layer. For the simplest case of a 1-layer substrate ($N=1$) extending to $z = -\infty$ (occupying a half-space),

$$Q_1(k_x) = \sqrt{k_x^2 + \gamma_1^2} \quad (9.10)$$

The quantity $\gamma_1^2 = j\omega\mu(\sigma_1 + j\omega\epsilon_1)$ is determined by the frequency (ω) and substrate properties.

The expressions for $Q_N(k_x)$ become increasingly cumbersome as the number of layers increases. The corresponding expressions for two- and three- layer substrates (the cases most often encountered) are:

$$Q_2(k_x) = m_1 \times \frac{(m_1 + m_2)e^{2m_1z_1} - (m_1 - m_2)}{(m_1 + m_2)e^{2m_1z_1} + (m_1 - m_2)} \quad (9.11)$$

$$Q_3(k_x) = m_1 \times \frac{1 - e^{-2m_1z_1}q(k_x)}{1 + e^{-2m_1z_1}q(k_x)}, \text{ with} \quad (9.12)$$

$$q(k_x) = \frac{\left[\begin{array}{c} (m_1 + m_2)(m_2 - m_3) + \\ (m_1 - m_2)(m_2 + m_3)e^{2m_2z_2} \end{array} \right]}{\left[\begin{array}{c} (m_1 - m_2)(m_2 - m_3) + \\ (m_1 + m_2)(m_2 + m_3)e^{2m_2z_2} \end{array} \right]}$$

In (9.11) and (9.12), z_1 refers to the thickness of the top substrate layer and z_2 the thickness of the second substrate layer (in the case of 3-layer substrate) while the last substrate layer extends to $-\infty$. The coefficients m_i , corresponding to the i^{th} substrate layer, are given by:

$$m_i(k_x) = \sqrt{k_x^2 + \gamma_i^2} = \sqrt{k_x^2 + j\omega\mu(\sigma_i + j\omega\epsilon_i)} \quad (9.13)$$

9.2.3. Discrete complex images. As described in the previous sub-section, the dipole Green's function expression is the sum of a *primary* term corresponding to the magnetic dipole source and a *secondary* term arising due to reflections at the interfaces in the substrate. While the primary term by itself is integrable and gives rise to the field of a static magnetic dipole, analytical computation of the entire integral is hampered by the coefficient χ_N . The key for computing the substrate Green's function lies in finding a suitable approximation to χ_N that transforms the secondary term into an analytically integrable form. The Discrete Complex Images Method (DCIM) [4], [16] is used to approximate χ_N with a linear combination of complex exponentials - an often favored approach for 3D problems:

$$\chi_N(k_x) \approx \sum_{j=1}^M b_j e^{c_j k_x} \quad (9.14)$$

Since the exponentials in (9.14) above readily combine with those in the secondary term in (9.7), (9.8), the substrate contribution to the Green's function takes a form identical to that of the source term. The sum of exponentials in (9.14) is interpreted

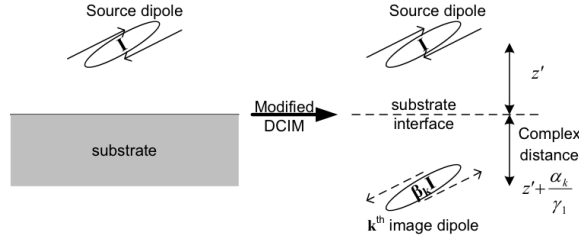


FIGURE 9.2.4. Physical interpretation of Modified Discrete Complex Images Method.

as a series of images of the source magnetic dipole. A challenge in this approach is to find a suitable set of 'complex images', c_j , that gives a sufficiently accurate Green's function in coordinate space. The accuracy requirements are determined a posteriori, with the computation of impedance parameters based on the Green's function. In 2D, the complete integrand of the term containing χ_N is a smooth function of the integration variable, which simplifies the demands for high accuracy in a parameterization of the form (9.14).

We use a simpler search that we motivate here with a new look at the form of the dipole Green's function (G) in the presence of a substrate. For a single-layer substrate, with $Q_1(k_x)$ given by (9.10), we can perform the following algebraic replacement:

$$\begin{aligned}\chi_1(k_x) &= e^{-2 \tanh^{-1} \left(k_x / \sqrt{k_x^2 + \gamma_1^2} \right)} \\ &= e^{-2 \tanh^{-1} \left((k_x / \gamma_1) / \sqrt{1 + (k_x / \gamma_1)^2} \right)} = e^{-2 \sinh^{-1} \left(\frac{k_x}{\gamma_1} \right)}\end{aligned}\quad (9.15)$$

This alternative functional representation of $\chi_1(k_x)$ naturally leads us to a separation of the coefficient $1/\gamma_1$ in the complex exponent. We preserve this coefficient and search for $\alpha_k \in \mathbb{R}$, and $\alpha_k > 0$ for convergence, while we allow the coefficients β_k to remain complex, thus:

$$\chi_1(k_x) \approx \sum_{k=1}^K \beta_k e^{-\alpha_k (k_x / \gamma_1)} \quad (9.16)$$

Pictorially, in (9.16) the k^{th} term represents an image of the dipole current source whose z -coordinate depends on α_k , as shown in Fig. 9.2.4, while the coefficient β_k emulates the fraction of the incident current carried by the k^{th} image. This interpretation results from $\sum_k \beta_k = 1$ - a consequence of $\chi_1(0) = 1$. The analogy for β_k would be exact with the added constraints $\beta_k \in \mathbb{R}$ and $\beta_k \in (0, 1)$. However, we do not impose these constraints to get higher accuracy. The detailed results and implications on accuracy of impedance extraction are addressed in more detail in the following section.

Inserting (9.16) into (9.7) and (9.8), results in:

$$\begin{aligned}
& G_{ver}^{d,R_0}(x, z, z') \\
& \approx - \int_0^\infty \left(\begin{array}{c} e^{-|z-z'|k_x} \\ - \sum_{k=1}^K \beta_k e^{-\alpha_k \frac{k_x}{\gamma_1}} e^{-(z+z')k_x} \end{array} \right) \sin(k_x x) dk_x \\
& = - \left[\frac{x}{|z-z'|^2 + x^2} - \sum_{k=1}^K \left(\beta_k \frac{x}{(z+z' + \frac{\alpha_k}{\gamma_1})^2 + x^2} \right) \right]
\end{aligned} \tag{9.17}$$

$$\begin{aligned}
& G_{hor}^{d,R_0}(x, z, z') \\
& \approx - \int_0^\infty \left(\begin{array}{c} e^{-|z-z'|k_x} \\ + \sum_{k=1}^K \beta_k e^{-\alpha_k \frac{k_x}{\gamma_1}} e^{-(z+z')k_x} \end{array} \right) \cos(k_x x) dk_x \\
& = - \left[\frac{|z-z'|}{|z-z'|^2 + x^2} + \sum_{k=1}^K \left(\beta_k \frac{z+z' + \frac{\alpha_k}{\gamma_1}}{(z+z' + \frac{\alpha_k}{\gamma_1})^2 + x^2} \right) \right]
\end{aligned} \tag{9.18}$$

We extend this restricted search for parameters (α_k, β_k) using (9.16) to 2-layer and 3-layer substrate configurations. Hence, for the general N-layer substrate:

$$\chi_N(k_x) \approx \sum_{k=1}^K \beta_k e^{-\alpha_k (k_x / \gamma_1)} \tag{9.19}$$

and the expressions (9.17), (9.18) remain valid. The set (α_k, β_k) of parameters only depend on the substrate profile (resistivity, dielectric constant and thickness of each layer) and the frequency of interest. The computation of these parameters constitutes a *one-time cost* for a given technology, at each frequency. We can use alternative fitting strategies, including Matlab's built-in 'fminsearch' and VARPRO, to compute the approximation (9.19).

9.2.4. Three-dimensional (3D) interconnect. When the conditions for a 2D treatment are not satisfied a 3D alternative is required. This is the case for the highly sensitive on-chip inductors which are typically designed as concentric spirals on a single or multiple metal layers. Each inductor forms a single current loop composed of an arrangement of segments electrically composed of several turns in series, with the segments being quite short compared to the wavelength, λ . In addition, the transverse separation between the segments of a loop are of the same order as the length of the segments, while the entire object can be of the order of λ . Such structures necessitate a 3D impedance computation.

9.2.5. Integral representation of the 3D Green's function. In 3D layered media, the Green's function for the vector potential can be written as a second rank tensor. Consider $\vec{\vec{G}}$, whose components are $G_{u,v}$, where u denotes the direction of the dipole source and v the direction of the resultant magnetic vector potential \vec{A} . For the three dimensional magnetic dipole formed by two opposite currents $I\hat{y}$ and $-I\hat{y}$, centered at (x', y', z') and separated by an infinitesimal distance a , the magnetic dipole moment is along \hat{z} . The \hat{y} -directed magnetic vector potential

at (x, y, z) in the region above the substrate ($\vec{A}_{z,y}^{d,R_0}$) due to this magnetic dipole, satisfies:

$$\begin{aligned} \nabla^2 \vec{A}_{z,y}^{d,R_0}(x, y, z, x', y', z') \\ = -\hat{y} \frac{\mu}{2\pi} (Ia) \times \frac{2\pi}{a} \begin{bmatrix} \delta(x - x' + \frac{a}{2}) \delta(y - y') \delta(z - z') - \\ \delta(x - x' - \frac{a}{2}) \delta(y - y') \delta(z - z') \end{bmatrix}; \quad (9.20) \\ z, z' > 0 \end{aligned}$$

In the region R_0 above the substrate, the corresponding \hat{y} -directed vector potential Green's function $G_{z,y}^{d,R_0}$ for a \hat{z} -directed unitary magnetic dipole source, with $I \rightarrow \infty$ and $a \rightarrow 0$ such that the dipole moment $|\vec{p}| = \frac{\mu}{2\pi} (Ia) = 1$, is:

$$\begin{aligned} G_{z,y}^{d,R_0}(x, y, z, x', y', z') = \frac{-\mu}{2(2\pi)^2} \times \\ \int_{-\infty}^{\infty} \int_{-\infty}^{\infty} \left(\frac{k_x}{k_z} e^{jk_x(x-x') + jk_y(y-y')} \left(e^{jk_z|z-z'|} + \chi_N(|k_z|) e^{jk_z(z+z')} \right) \right) dk_x dk_y; \\ k_z = j \sqrt{k_x^2 + k_y^2} \quad (9.21) \end{aligned}$$

9.2.6. 3D Green's function with complex images. While several techniques have been proposed to implement DCIM to approximate the 3D substrate Green's function [4],[8], [12],[19], [27], it has been considered a challenging task [4], [26]. Two features have been widely mentioned in the literature as limitations of the DCIM [4], [5]. The first is the use of uniform sampling rate in the spectral variables k_x , k_y requiring either very fine sampling in k_x , k_y or different DCIM parameterizations, to capture steep variations in the fitted function χ_N for typical multi-layer substrates. The second is its sensitivity to the signal frequency interval.

We found that with the constraint $\alpha_k \in \mathbb{R}$ the impedance computation did not yield accurate results. On relaxing this constraint to allow $\alpha_k \in \mathbb{C}$, we found that the 'fminsearch' algorithm in Matlab did not yield an accurate set of 'complex images'. However, the VARPRO method once extended to the complex domain, yields the desired level of accuracy as shown in Sections 9.4 and 9.5.

The analytical expressions for the 3D vector potential Green's function with complex images are simple to obtain. For example, the y-directed component of the Green's function for a z-directed 3D magnetic dipole in free space is known in closed form [17]:

$$G_{z,y}^{d,free} = \frac{\mu}{4\pi} \frac{(x - x')}{[(x - x')^2 + (y - y')^2 + (z - z')^2]^{3/2}} \quad (9.22)$$

and the equivalent expression for a 3D magnetic dipole lying above a multi-layer substrate is:

$$\begin{aligned} \bar{G}^{d,sub}(x, y, z, x', y', z') \\ = \bar{G}^{d,free}(x, y, z, x', y', z') + \sum_{k=1}^K \beta_k \bar{G}^{d,free}(x, y, z, x', y', -z' - \frac{\alpha_k}{\gamma_1}) \quad (9.23) \end{aligned}$$

9.3. Impedance computations

The Green's functions discussed in the previous section are solutions to the vector potential due to a unit magnitude dipole source located at a point $\vec{r}' = (x', y', z')$. To compute the vector potential at any point $\vec{r} = (x, y, z)$ due to a finite size current loop, we can consider the finite loop as a superposition of infinitesimally small point sources in the area occupied by the current loop, each having a loop area $\frac{1}{2}(dx' \times dy')$ and carrying current I . The co-ordinates of the source (x', y', z') span the rectangular (shaded) area shown in Fig. 9.2.3, whose extremities are defined by (x_1, y_1, z_1) , (x_1, y_2, z_1) , (x_2, y_1, z_2) and (x_2, y_2, z_2) . Expressing the z-coordinate of the source in terms of x' and ϕ : $z_{x'} = z_1 + (x' - x_1)\tan(\phi)$, the vector potential at $\vec{r} = (x, y, z)$ due to the finite current loop in free space is given by:

$$\begin{aligned} \vec{A}^{d,free}(x, y, z) &= \hat{y} \left(A_{G_{x,y}}^{d,free}(x, y, z) + A_{G_{z,y}}^{d,free}(x, y, z) \right) + \hat{x} A_{G_{z,x}}^{d,free}(x, y, z) \end{aligned} \quad (9.24)$$

where each $A_{G_{u,v}}^{d,free}$ is given by:

$$A_{G_{u,v}}^{d,free}(x, y, z) = \int_{y_1}^{y_2} \int_{x_1}^{x_2} G_{u,v}^{d,free}(x, y, z, x', y', z_{x'}) I dx' dy' \quad (9.25)$$

For the particular choice of co-ordinates used here (currents along \hat{y}), the term $A_{G_{z,x}}^{d,free} = 0$. As expected, the resultant magnetic vector potential is directed along \hat{y} , just as the currents in the source loop. In the presence of a multi-layer substrate, $\vec{G}^{d,free}$ in (9.24) must be replaced by $\vec{G}^{d,sub}$ from (9.23), which gives:

$$\begin{aligned} \vec{A}^{d,sub}(x, y, z) &= \int_{y_1}^{y_2} \int_{x_1}^{x_2} \vec{G}^{d,free}(x, y, z, x', y', z_{x'}) \cdot \vec{p}(\vec{r}') dr' \\ &+ \sum_{k=1}^K \beta_k \int_{y_1}^{y_2} \int_{x_1}^{x_2} \vec{G}^{d,free}(x, y, z, x', y', z_{x'}^k) \cdot \vec{p}(\vec{r}') dr' \end{aligned} \quad (9.26)$$

where $z_{x'}^k = -(z_1 + \alpha_k/\gamma_1) + (x' - x_1)\tan(\phi)$ is the z-coordinate of the k^{th} image dipole, and the angle ϕ is shown in Fig. 9.2.3.

For filament currents, or finite cross-sections with uniform current density, the mutual inductance between the source current loop and a victim conductor is given by:

$$M = \psi/I = \oint_l \vec{A}(\vec{r}) \cdot d\vec{l}/I \quad (9.27)$$

where $d\vec{l}$ is the length vector for an infinitesimal element of the victim conductor, \vec{r} is the position vector for this element, ψ is the magnetic flux generated by the source current integrated over the surface of the victim current. The Stokes theorem is used to express the flux of the magnetic field \vec{B} as the circulation of \vec{A} along the boundary of the victim current and \vec{l} is the contour along the conductor length. For a victim conductor oriented along \hat{y} extending from (x_3, y_3, z_3) to (x_3, y_4, z_3) , (9.27) becomes:

$$M_y^{d,sub} = \int_{y_3}^{y_4} \vec{A}^{d,sub}(x_3, y, z_3) \cdot d\hat{y}/I \quad (9.28)$$

All the integrals shown above can be evaluated in closed form.

The exact expressions for $M_{G_{x,y}}^{d,free}$ and $M_{G_{z,y}}^{d,free}$ are:

$$\begin{aligned}
M_{G_{x,y}}^{d,free} &= \frac{\mu}{4\pi} \left[\left[\left[M_{G_{z,y}}^{d,free} \tan^2(\phi) + q \right]_{y'=y_1}^{y'=y_2} \right]_{x'=x_1}^{x'=x_2} \right]_{y=y_3}^{y=y_4} ; \\
M_{G_{z,y}}^{d,free} &= \frac{\mu}{4\pi} \cos^2(\phi) \\
&\times \left[\left[\left[\frac{\cos(\phi)}{2} \left(v \ln \left| \frac{\sqrt{m^2+v^2}-v}{\sqrt{m^2+v^2}+v} \right| + 2\sqrt{m^2+v^2} \right) - q \right]_{y'=y_1}^{y'=y_2} \right]_{x'=x_1}^{x'=x_2} \right]_{y=y_3}^{y=y_4} ; \\
q &= \sin(\phi) \left(z_k \cos(\phi) \tanh^{-1} \left(\frac{t}{\sqrt{m^2+v^2}} \right) + v \tan^{-1} \left(\frac{t}{z_k \cos(\phi) \sqrt{m^2+v^2}} \right) \right) ; \\
u &= x_3 - x' ; v = y - y' ; z_k = (z_3 - z_1) - (x_3 - x_1) \tan(\phi) ; \\
t &= u \sec(\phi) + z_k \sin(\phi) ; m^2 = t^2 + z_k^2 \cos^2(\phi)
\end{aligned} \tag{9.29}$$

In the presence of a multi-layer substrate, the mutual impedance $M_y^{d,sub}$ for a filament (the corresponding procedure for an interconnect comprising multiple filaments is explained in [25]) can be reduced to a closed form quadrature when using a linear combination of exponentials on the integrand as in 2D, thus:

$$M_y^{d,sub} = M_{G_{x,y}}^{d,free} + M_{G_{z,y}}^{d,free} + \sum_{k=1}^K \beta_k (M_{G_{x,y}}^{d,img} + M_{G_{z,y}}^{d,img}) \tag{9.30}$$

where $M_{G_{x,y}}^{d,img}$ and $M_{G_{z,y}}^{d,img}$ are given by the same expressions as those for $M_{G_{x,y}}^{d,free}$ and $M_{G_{z,y}}^{d,free}$, respectively, with the following modification to (9.29):

$$z_k = (z_3 + z_1 + \alpha_k / \gamma_1) - (x_3 - x_1) \tan(\phi) \tag{9.31}$$

The results presented here are sufficient to compute the *mutual* impedance of Manhattan interconnects of filament loops by orienting the co-ordinate axes such that relevant conductors are parallel to \hat{y} . We now discuss the changes needed to compute diagonal elements of the impedance matrix, as in computing the *self* inductance of a loop, in which case the victim loop coincides with the source. Since the center-to-center distance between the source and destination points $u = x_3 - x'$ in (9.29) is zero, the self-inductance is computed by replacing the distance $u = x_3 - x' = 0$ with the geometric mean distance (GMD) [14] of the conductors. The GMD of a rectangular cross-section conductor with respect to itself is given by $e^{\log(w+t)-3/2}$ [14]. The self impedance is then given by $Z_{self} = R_{self} + j\omega M_{self}$, where $R_{self} = \rho L \left(\frac{1}{w_{s_1} t_{s_1}} + \frac{1}{w_{s_2} t_{s_2}} \right)$ is the static resistance of the signal line (s_1) and return path (s_2) of the loop (w_{s_1}, w_{s_2} are widths and t_{s_1}, t_{s_2} are the thicknesses of the conductors).

9.3.1. Non-Manhattan interconnects. Besides Manhattan interconnects, it is of primary interest to compute the impedance of inductors, which may comprise conductor segments inclined at arbitrary angle θ . In this case, we choose a co-ordinate system that aligns the source current loop with \hat{y} . For the victim conductor extending from (x_3, y_3, z_3) to (x_4, y_4, z_3) , the x-coordinate can be expressed in terms of its y-coordinate as: $x_y = x_3 + (y - y_3) \tan(\theta)$. The mutual impedance is

then given by (9.32). For conductor loops in the $\hat{x} - \hat{y}$ plane ($\phi = 0$), the integral in (9.32) also leads to closed form quadratures, albeit the resulting expression is too long to be included in this chapter.

$$\begin{aligned}
M_{\theta}^{d,free} &= \frac{\mu}{4\pi} \int_{y_3}^{y_4} I_y dy; \\
I_y &= \cos(\phi) \left[\left[-\sinh^{-1} \left(\frac{y - y'}{\sqrt{(x_y - x')^2 + (z_3 - z_{x'})^2}} \right) \right]_{x'=x_1}^{x'=x_2} \right]_{y'=y_1}^{y'=y_2} \\
&+ \sin(\phi) \left[\left[\tan^{-1} \left(\frac{(x_y - x')(y - y')(z_3 - z_{x'})^{-1}}{\sqrt{(x_y - x')^2 + (y - y')^2 + (z_3 - z_{x'})^2}} \right) \right]_{x'=x_1}^{x'=x_2} \right]_{y'=y_1}^{y'=y_2}; \\
x_y &= x_3 + (y - y_3)\tan(\theta)
\end{aligned} \tag{9.32}$$

9.4. Least square fits for multi-layer substrates

The modified discrete complex images approximation [25], shown in (9.16), allows us to represent the effect of the substrate as the combined effect of a series of images of the source magnetic dipole. The advantage of this representation is evident from the convenient analytical expressions for mutual impedance shown in the previous section. The accuracy of this approximation is the key element for computing the effect of substrate eddy current effects on interconnect impedance. For simpler 2D interconnect configurations we compute the discrete complex images with $\alpha_k \in \mathbb{R}, \beta_k \in \mathbb{C}$, using Matlab's built-in function 'fminsearch' with reasonable accuracy. In the general 3D case, when the current loops are wide, and the transverse separation of a signal line from its return path is much larger than the height of the interconnects above the substrate, the effect of the substrate is much more pronounced. The need for higher accuracy in such cases dictates that $\alpha_k \in \mathbb{C}$, resulting in a larger set of unknown parameters. In this case, the 'fminsearch' algorithm does not yield good results. The Variable Projections algorithm [13], on the other hand, inherently reduces the number of unknowns in the least square fit and provides a much better approximation with reasonable computation time. The VARPRO algorithm combined with the modified DCIM, which provides a good initial guess for the non-linear parameters in the exponents, extends several desirable properties to the exponential fits as shown below. In the following paragraphs we first describe the basic principle of the VP algorithm and then outline the procedure for obtaining accurate complex image approximations for multi-layer substrates employing this algorithm.

9.4.1. Variable Projection method for non-linear least squares fitting. The search for an accurate set of images (α_k, β_k) for a particular substrate configuration at frequency ω constitutes a non-linear least squares problem - we seek values for α_k and β_k so as to minimize the sum of the squares of the discrepancies between the right and left hand sides of (9.16), for all values of the Fourier transform variable $k_x \in (0, \infty)$. Exact expressions for $\chi_N(k_x)$ (subsequently referred to simply as χ , for conciseness) are known [25], in terms of k_x , for each frequency. Hence, for a set of J observation points in $(0, \infty)$, we have a vector of

observations $\{k_{xj}, \chi_j; k_{xj} \in (0, \infty)\}$ as the input data set to the following non-linear least squares problem:

$$\min_{\beta, \alpha} \sum_{j=1}^J \left[\sum_{k=1}^K (\beta_k \phi(\alpha_k, k_{xj}) - \chi_j)^2 \right] \quad (9.33)$$

α_k and β_k are the parameters to be determined such that the discrepancy of the model $\beta_k \phi(\alpha_k, k_{xj})$ with respect to the complex observations χ_j is minimized.

Since this is a non-linear non-convex problem in general, it can have multiple solutions. Writing the $J \times K$ matrix $\{\phi(\alpha_k, k_{xj})\}$ as Φ and the vector of observations $\{\chi_j\}$ as \mathbf{x} , the vector residual in (9.33) is concisely represented as:

$$\mathbf{r}_2(\alpha) = \Phi(\alpha)\beta - \mathbf{x} \quad (9.34)$$

Now, for each fixed value of α , (9.34) is a linear least squares problem, whose solution can be explicitly written as:

$$\beta = \Phi^+(\alpha)\mathbf{x}, \quad (9.35)$$

where $\Phi^+(\alpha)$ is the pseudo-inverse of Φ . Replacing this expression in (9.33), the original non-linear least squares problem becomes:

$$\min_{\alpha} \|\mathbf{I} - \Phi(\alpha)\Phi^+(\alpha)\| \|\mathbf{x}\| \quad (9.36)$$

Since $\mathbf{I} - \Phi(\alpha)\Phi^+(\alpha) = P_{\Phi(\alpha)}^\dagger$ is the projector on the subspace orthogonal to the column space of Φ , (9.36) has been called the Variable Projection (VP) functional. An obvious gain by this procedure, as opposed to the initial problem, is a reduction in the number of variables, since the linear parameters (β_k) have been eliminated from the problem.

9.4.2. Complex images using Variable Projection algorithm. The VP algorithm described above is applied to solve the non-linear least squares problem to determine the complex images in terms of the best fit parameters α_k and β_k . We allow values $(\alpha_k, \beta_k) \in \mathbb{C}$. To ensure a good fit, the VP algorithm naturally satisfies the requirements that $\text{Re}(\alpha_k) > 0$ (for convergence) and $\sum_k \beta_k = 1$ (which is a property of the input data, χ). Fig. 9.4.1 shows the fits for a single layer ($N = 1$) substrate. Before the VP algorithm is applied to solve the non-linear least squares problem, two choices must be made: the number of exponentials (K) in the model (the number of complex images), and the initial values for the non-linear parameters α_k .

In general, increasing the number of images improves the accuracy of the approximation, while simultaneously increasing the cost of computation. However, we find that the choice of initial values for the parameters α_k has a much greater bearing on the accuracy of the approximation than the number of images. As explained in the previous sub-section, the Variable Projection method eliminates the need to guess initial values for the linear parameters β_k . We are interested in complex image representations of the substrate over a wide range of frequencies (20-100 GHz). Since we expect from the modified DCIM that the exponential parameters lie in the vicinity of the complex number $1/\gamma_1$ [25], we start at one end of the frequency spectrum (say 100 GHz) using random values between 0 and 1 as initial guesses for α_k . The best fit values for α_k obtained from the VP algorithm at this frequency are used as the initial guess for an adjacent frequency point. Since

χ is a smooth function of ω , the best fit values for α_k obtained from the VP algorithm at this frequency provide a good initial guess for the parameters at the next adjacent frequency, as long as the next frequency point is close enough to the first. This strategy of "continuation" in frequency is applied progressively over the entire frequency range of interest. If the desired level of accuracy is not achieved for all frequency points, this process should be repeated across the frequency range by choosing as initial values the parameters at the frequency point with minimum residual error. This procedure is summarized in Figure 9.4.2.

The residual errors and the computation time to perform the fit (9.19) is shown in Fig. 9.4.3, as a function of the number of complex images. Our algorithm results in a fit that is smooth as a function of frequency, in terms of the residual error of the fit (Fig. 9.4.4). Finally, Fig. 9.4.5 shows the error in the Green's function computation using the simplified discrete complex images approximation, for a large number of randomly generated technology parameters.

9.5. Impedance computation results

In this section, we show results of the impedance extraction method that incorporates the discrete complex images for a multi-layer substrate computed using the VARPRO algorithm. Through comparisons with electromagnetic field solvers, we demonstrate the accuracy as well as computational efficiency of the proposed method.

9.5.1. 2D interconnect structures. Fig. 9.5.1(a) plots the self-impedance and the mutual impedance of two conductor loops on different metal layers with a vertical separation of $1\mu m$, while Fig. 9.5.1(b) plots the error in the computation with respect to the magneto-quasi-static (MQS) electromagnetic field solver FastHenry [18]. The dashed lines in Fig. 9.5.1(b) show the significant error in impedance if the substrate were to be neglected - as much as 20% at 100 GHz. It is found that the proposed method captures the effect of the substrate on interconnect impedance with high accuracy (solid lines show errors less than 2%) in the entire frequency range of interest for digital circuits. Note that in this and

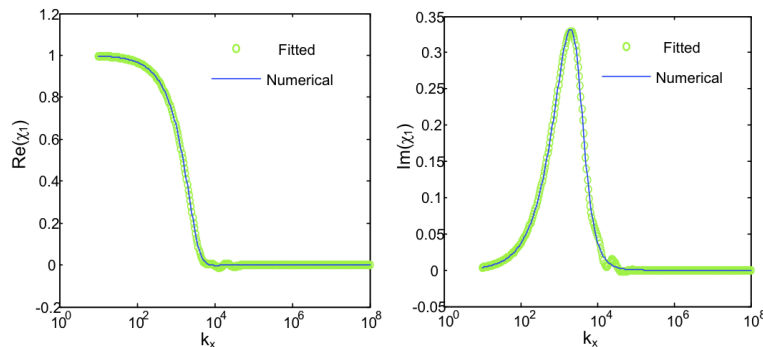


FIGURE 9.4.1. Approximation of the Real and Imaginary parts of χ_1 using our exponential fits with $K = 20$, for a single-layer substrate $\rho = 10hm - cm$, in comparison with numerical computation.

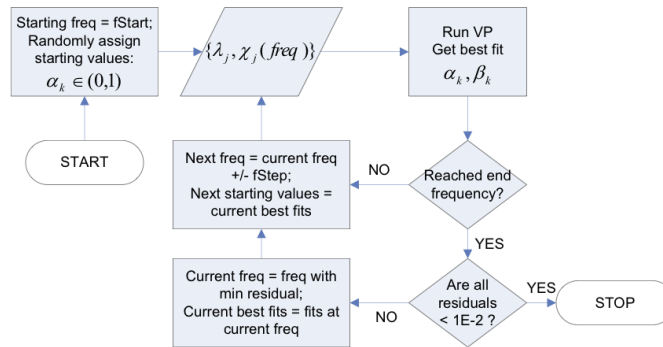


FIGURE 9.4.2. Algorithm flowchart for computing complex image approximation using Variable Projections.

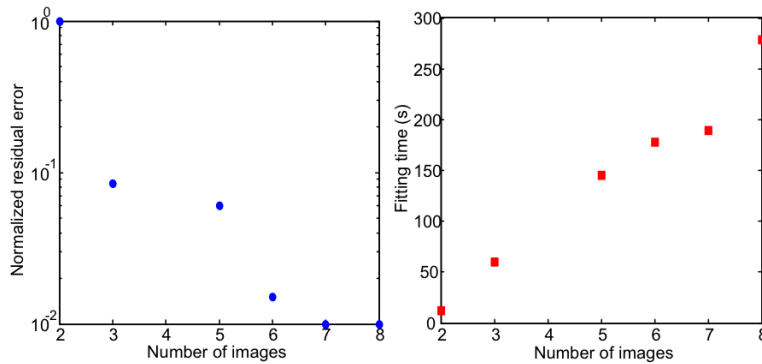


FIGURE 9.4.3. (a) Residual error (normalized to the error using 2 images), and (b) computation time, as a function of the number of complex images, for a 1-layer substrate at one frequency point (90 GHz).

all subsequent experiments, the conductors are always discretized into filaments to capture non-uniform current distribution within the conductors.

We now compare the network Z-parameter (Z_{in}) for a conductor loop, to that obtained from the commercial full-wave field solver, HFSS [1]. The Z_{in} parameter is computed by using a Spice distributed transmission line model, wherein the resistance and inductance per unit length are computed by using our method, and the capacitance is obtained from FastCap [20]. The geometry simulated with HFSS is shown in Fig. 9.5.2 (inset).² The results of the comparison are shown in Fig. 9.5.2. The maximum error observed in the magnitude of Z_{in} for this configuration is less than 2%. Note that for frequencies beyond 60 GHz the results from HFSS become unstable for the configuration shown.

² The conductor loop is closed by including additional metal strips at the far and near ends of the loop. The effect of the additional metal is insignificant since the length of the conductors is much larger than the transverse separation between them. A small gap ($0.2\mu m$) is left at the near end where a lumped port excites the conductor loop.

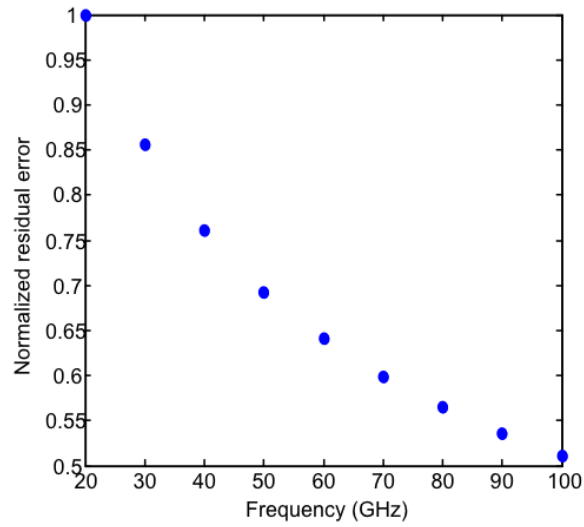


FIGURE 9.4.4. Residual error (normalized to the error at 20 GHz) in the sum of complex exponentials fit for a 3-layer substrate with 5 complex images, as a function of frequency.

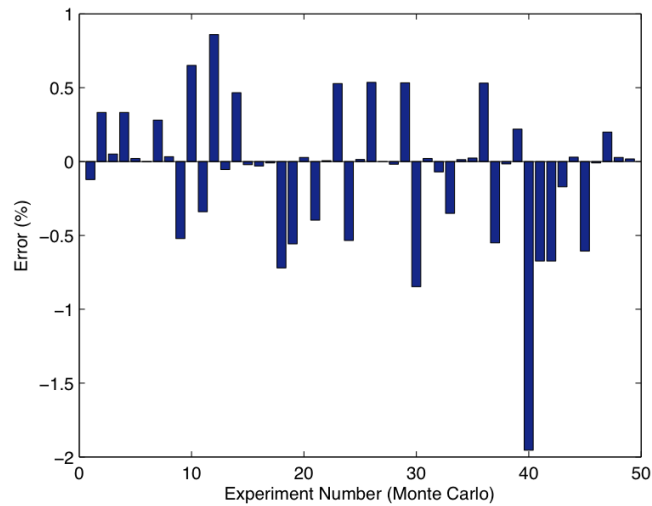


FIGURE 9.4.5. Error in the co-ordinate space representation of the dipole Green's function computation using 5 images, with respect to numerical computation for a 3-layer substrate. Monte Carlo simulations are done for: frequency 20 to 100 GHz, z-separation 0.5 to 1.0 μm , x-separation 0.5 to 10 μm .

Fig. 9.5.3 shows a long Manhattan wire with orthogonal segments running on adjacent metal layers M10 and M11, along with a regular grid of ground wires. Each segment of the signal line is routed in close proximity to a segment of the ground

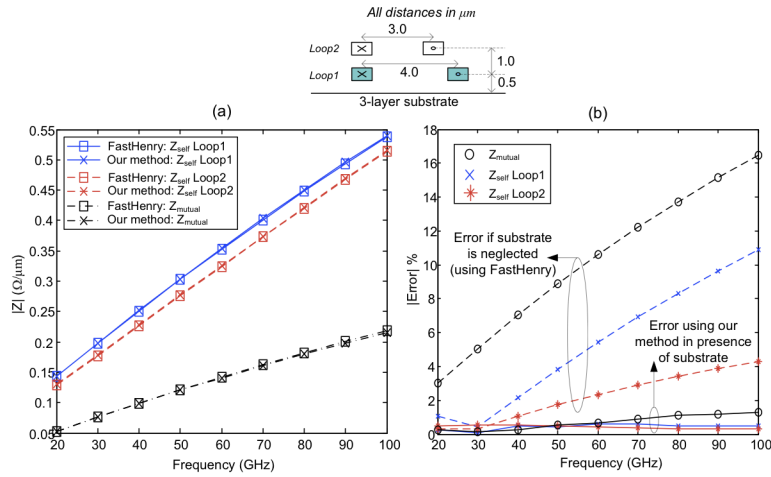


FIGURE 9.5.1. (a) Self and mutual impedance for two conductor loops lying on different metal layers above the three-layer substrate, as a function of frequency. (b) % error in magnitude of impedance using our method in comparison with FastHenry (solid lines), and the error in impedance if the substrate was to be neglected (dashed lines).

grid on the corresponding metal layer - a common design for timing-critical global interconnects to control inductive effects. The mutually perpendicular segments of the Manhattan wire are decoupled (for example, segments AB and BC). On the other hand, the mutual impedance between far apart parallel segments AB-CD (or between BC-DE) can be neglected because of the large separation ($100\mu\text{m} - 200\mu\text{m}$) between them. Hence, we can separately apply our approach to each linear segment (AB, BC, CD and DE, respectively) to obtain the impedance of the Manhattan wire. As shown in Fig. 9.5.3 our results have a maximum error about 2% over the entire frequency range of interest.

Further experiments using Monte-Carlo simulations for a large number of randomly generated interconnect geometries for global wires at the 45 nm node [2] over a wide range of frequencies show a maximum error of 2.3% (Fig. 9.5.4).

With prevalent methods for interconnect impedance computation that are based on the free space Green's function, for example FastHenry, the substrate layers must be included as explicit conductors. At relevant high frequencies, these layers must also be discretized into a large number of filaments (in addition to the interconnects) to capture the substrate eddy currents for a general interconnect configuration. The use of such methods is thus limited to relatively small structures such that the size of the resulting linear system including the multi-layer substrate does not overwhelm available memory. Our method for impedance computation is based on analytical expressions for the substrate Green's function, wherein the substrate boundary conditions are implicit. The only filaments that need to be considered in the solution are those corresponding to the interconnects themselves.

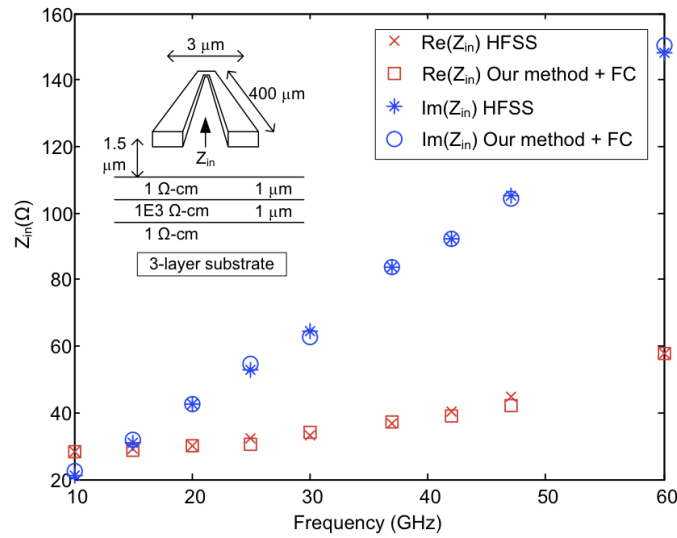


FIGURE 9.5.2. Impedance (Z_{in}) of the one-port network formed by a closed conductor loop (shown in inset) above a 3-layer substrate, compared with HFSS [1]. The indexmagneto-quasi-static impedance obtained using our method is combined with capacitance from FastCap (FC) [20] using a transmission line model in Spice to obtain the Z_{in} parameter. Conductor width $1\mu m$, thickness $0.5\mu m$, each sub-divided into 15 filaments for impedance computation.

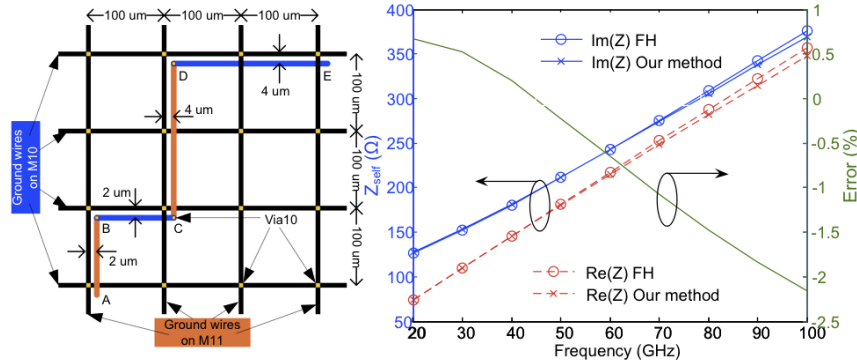


FIGURE 9.5.3. Impedance of a Manhattan interconnect laid out on metal layers M10 (blue) and M11 (orange) above a 3-layer substrate. A grid of ground wires provides nearby return paths to each wire segment. Interconnect geometry parameters are as per global wires at the 45 nm node [2].

Fig. 9.5.4(b) shows the speedup in self-impedance computation using our method with respect to a standard MQS computation where the substrate is represented using 2D filaments, as observed from Monte-Carlo simulations on a large

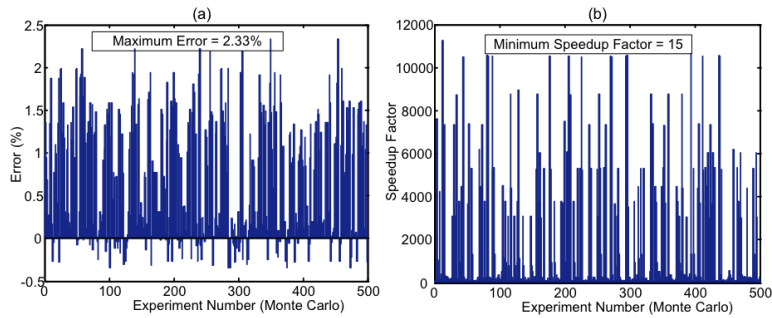


FIGURE 9.5.4. (a) Error in loop self impedance computation with respect to FastHenry, and (b) speedup in runtime with respect to a MQS computation with the substrate represented as 2D filaments, during Monte Carlo simulation of several randomly generated conductor configurations according to the following parameters: Frequency 20-100 GHz, pitch 2-8 μm , wire width 1-2 μm , height above substrate 1.5-2.2 μm (corresponding to metal layers M10 through M12). Interconnect geometry parameters correspond to global wires at the 45 nm node [2].

number of randomly selected interconnect geometries. In these experiments, our method is found to be at least 15 times faster. In the 2D MQS computation, the substrate must be discretized into a sufficient number of thin filaments so as to ensure that the filament cross-sections are smaller than the skin depth at the specified frequency. As a result, when the thickness of the low-resistivity top layer of the substrate increases to a few μm [3], the computation cost increases substantially due to the larger number of filaments required. On the other hand, with our method a change in the substrate layer thickness only demands evaluation of a new set of substrate images while the impedance computation cost remains constant. As a result, Table 1 shows orders of magnitude improvement in computational efficiency by using the analytical Green's functions.

9.5.2. 3D interconnect structures. Fig. 9.5.5(a) shows the computation for a single-turn square inductor configuration composed of two orthogonal loops (*loop-x* and *loop-y*, shaded with different colors). In this case, the net impedance Z of the square is given by a series combination of the two loops. Note that orthogonal loops have no mutual impedance. The results are plotted separately for the real and imaginary parts of Z . As frequency increases, the deviation in the plots with and without the substrate shows the significance of the substrate eddy current effects. Our computation agrees well with FastHenry over the entire frequency range, with a maximum error in $|Z|$ of less than 2%.

To compare our results with the input impedance for the interconnect structure obtained from the full-wave field solver HFSS [1], the capacitance (frequency independent) is extracted separately using FastCap [20]. Fig. 9.5.5(b) shows the network input impedance (Z_{in}) for the single-turn square inductor (found by simulating the circuit shown using HSPICE®), in comparison with the result obtained

TABLE 1. Computation cost for self impedance extraction of a 2-conductor loop over a $500\mu m$ wide 3-layer substrate, each conductor $1\mu m$ wide and $0.5\mu m$ thick, at 100 GHz. Substrate profile is shown in Fig. 9.5.2. z_1 : thickness of top substrate layer; F_{cond} : number of filaments per conductor; F_{sub} : number of filaments for substrate; T_i : time to compute images (one time cost); T_Z : time to compute impedance.

z_1	Substrate representation	F_{cond}	F_{sub}	T_i (s)	T_Z (s)
$1\mu m$	2D filaments	15	1323	-	110.2
	Analytical Green's function	15	0	90.6	< 1 sec
$2\mu m$	2D filaments	15	1952	-	313.7
	Analytical Green's function	15	0	107.1	< 1 sec
$3\mu m$	2D filaments	15	2581	-	821.5
	Analytical Green's function	15	0	166.9	< 1 sec
$4\mu m$	2D filaments	15	3829	-	2816
	Analytical Green's function	15	0	75.2	< 1 sec
$5\mu m$	2D filaments	15	4468	-	4522
	Analytical Green's function	15	0	146.8	< 1 sec

from HFSS. In this case, the maximum error in $|Z|$ is less than 3%, with some discrepancy in the real part of Z beyond 60 GHz due to corner effects not incorporated in our method, and the MQS approximation.

The time taken for relevant parts of the impedance computation are shown in Fig. 9.5.6. Evidently, our code takes a fraction of the time taken by FastHenry for the MQS computation, This is despite the fact that FastHenry uses an accelerated method with $O(N \log N)$ complexity for solving the linear system, while we use a direct method with $O(N^3)$ complexity. This leaves significant room for further improvement in runtime by the use of accelerated methods to solve the linear system, although these are not discussed here. In comparison with the full-wave field solver, our method gives almost an order of improvement in runtime for impedance computation at each frequency point (not including the runtime for calculating the complex images corresponding to the substrate profile once per technology generation, capacitance extraction once per interconnect geometry, and for HSPICE® simulation to compute Z_{in}).

Fig. 9.5.7 shows the impedance computation for a 3-turn spiral inductor, where each turn is a square. In this case, the self impedance of each turn is computed as explained in Fig. 9.5.5(a). In addition, the mutual impedance between all the turns need also be considered. The mutual impedance computation between parallel two-conductor loops has been derived in Section 9.3, while the mutual impedance between perpendicular loops is zero.

Finally, Fig. 9.5.8 shows the impedance of a 3-turn spiral inductor where each turn is an octagon. In this case, each octagon is composed of four loops: one each oriented along \hat{x} and \hat{y} , and two others inclined at 45° angles to each of these. While the mutual inductance between mutually orthogonal loops is zero, that between inclined loops must be computed as per (9.32). The maximum error in computing the magnitude of impedance $|Z|$ for this inductor using our method is 3% with respect to FastHenry.

9.6. Conclusions

In this chapter we have analyzed a computational problem of significant relevance to the analog integrated circuit design community. For wireless chips used in automotive sensors, digital radios and other high frequency devices, great care is needed to design accurate multiple inductor structures that show up in low noise amplifiers and other design components. The palette of tools available to the designer are three-dimensional Finite Element (time domain or frequency domain) electromagnetic solvers, whose capacity and CPU cost limit the broadband simulations of critical passive components. We have presented a system level approach based on analytical expressions for filling up the impedance matrix of the system for a broadband spectrum extending from near DC to 100 GHz. In doing so, we have restricted our attention to the most significant and computationally most expensive phenomena - those associated with the multi-layer substrate in the upper part of the frequency spectrum. We have demonstrated that the extension of VARPRO to complex non-linear parameters permits accurate fits of the reflexion coefficients for complex layered substrate configurations that are common in Silicon-based nanometer integrated circuit technologies. The fits involve a linear combination of complex exponentials with a small number of non-linear parameters. The fits at different frequencies involve solving separate non-linear optimization problems.

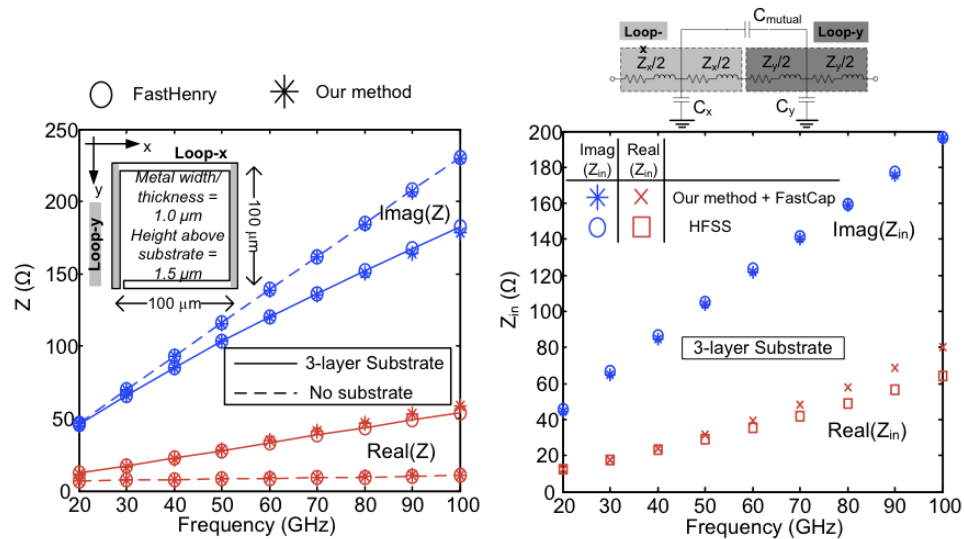


FIGURE 9.5.5. (a) Impedance of a single-turn square inductor as a function of frequency, with (solid lines) and without (dashed lines) the substrate, in comparison with FastHenry. (b) Input impedance network parameter Z_{in} for a square interconnect loop above a 3-layer substrate, as a function frequency, in comparison with HFSS [1]. Z_{in} is computed from the equivalent circuit shown above, using Spice, where the impedance (R, L parameters) are computed using our method and the capacitance elements are obtained from FastCap [20]. Substrate profile is the same as in Fig. 9.5.2.

	Full wave	MQS: R/L		Populating [Z]	Solving linear system
	HFSS	FH	Our method		
Time (s)	1230	927	146	8 s	138 s

FIGURE 9.5.6. Time taken for MQS impedance computation using FastHenry and our method, and full-wave computation using HFSS, at 100 GHz, for the example shown in Fig. 9.5.5. For our method, the time taken for the two steps - populating the impedance matrix and solving the corresponding linear system - is also shown separately.

The smoothness of the solution space, as indicated in Figures 9.4.3(a) and 9.4.4, guarantees the robustness of the approach. The chosen functional form ensures a

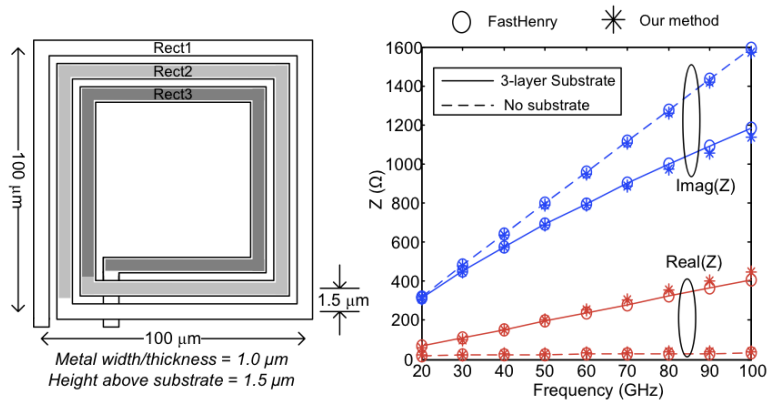


FIGURE 9.5.7. Impedance of a three-turn square inductor as a function of frequency, with and without substrate, in comparison with FastHenry. Substrate profile is the same as in Fig. 9.5.2.

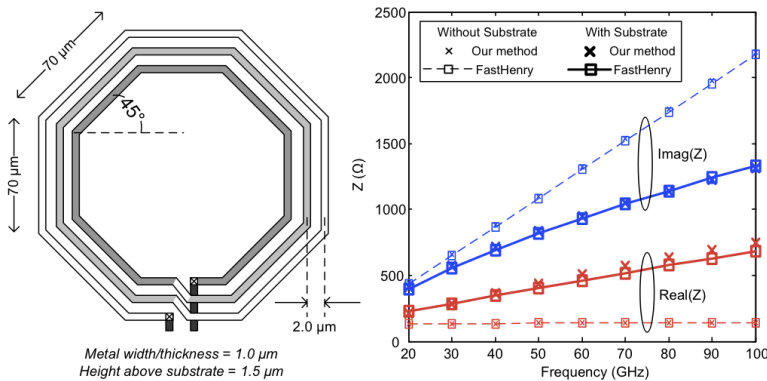


FIGURE 9.5.8. Impedance of a three-turn octagonal inductor as a function of frequency, with and without substrate, in comparison with FastHenry. Substrate profile is the same as in Fig. 9.5.2.

closed-form solution for the impedance matrix, which is related to the initial fit through a two-dimensional Fourier transform followed by a three dimensional integral over the coordinates of the conductors. It is altogether remarkable that for the physical conductors with rectangular cross sections and otherwise complex geometrical paths, as in for example in the case of general planar inductors, one can reduce the overall result to tractable analytical computations. The computational advantage of this analytical method over an electromagnetic field solver is evident from the analysis of Manhattan and non-Manhattan interconnects and inductors. From an accuracy perspective, the relatively lower sensitivity of impedance of two-dimensional structures to the accuracy of the fits for the reflection coefficient allows the use of simpler fitting algorithms than VARPRO. However, for three-dimensional structures where the sensitivity of the impedance to the accuracy of the reflection coefficient fits is large, VARPRO plays an important role in achieving the requisite levels of accuracy that cannot be achieved using alternative methods. With the increasing demand for complex wireless applications beyond 60 GHz frequency based on Silicon technologies, our efficient and accurate method offers a valuable solution for enabling designs in this frequency domain.

Bibliography

1. *User's Guide: HFSS v10.0*, Ansoft Corporation, 2005.
2. <http://www.itrs.net/reports.html>, ITRS, 2007.
3. <http://www.soitec.com/en/products/>, SOITEC, 2008.
4. M.I. Aksun, *A robust approach for the derivation of closed-form Green's functions*, IEEE Transactions on Microwave Theory and Techniques **44** (1996), no. 5, 651–658.
5. M.I. Aksun and G. Dural, *Clarification of issues on the closed-form Green's function in stratified media*, IEEE Transactions on Antennas and Propagation **53** (2005), no. 11, 3644–3653.
6. M. Born and E. Wolf, *Principles of Optics: Electromagnetic Theory of Propagation, Interference and Diffraction of Light*, Cambridge University Press, 1999.
7. W.C. Chew, *Waves and Fields in Inhomogeneous Media*, IEEE Press, New York, 1995.
8. Y.L. Chow, J.J. Yang, and G.E. Howard, *Complex images for electrostatic field computation in multilayered media*, IEEE Transactions on Microwave Theory and Techniques **39** (1991), no. 3, 1120–1125.
9. L. Daniel, *Simulation and Modeling Techniques for Signal Integrity and Electromagnetic Interference on High Frequency Electronic Systems*, Ph.D. thesis, University of California, Berkeley, CA, 2003.
10. A. Deutsch, G. Kopcsay, P. Restle, H. Smith, G. Katopis, W. Becker, P. Coteus, C. Surovic, B. Rubin, R.P.Jr Dunne, T. Gallo, K. Jenkins, L. Terman, R. Dennard, G. Sai-Halasz, B. Krauter, and D. Knebel, *When are transmission-line effects important for on-chip interconnections?*, IEEE Transactions on Microwave Theory and Techniques **45** (1997), no. 10, 1836–1846.
11. R. Escovar, S. Ortiz, and R. Suaya, *An improved long distance treatment for mutual inductance*, IEEE Transactions on Computer-Aided Design of Integrated Circuits and Systems **24** (2005), no. 5, 783–793.
12. D.G. Fang, J.J. Yang, and G.Y. Delisle, *Discrete image theory for horizontal electric dipoles in a multilayered medium*, IEE Proceedings H **135** (1988), no. 5, 297–303.
13. G. Golub and V. Pereyra, *The differentiation of pseudo-inverses and nonlinear least squares problems whose variables separate*, SIAM Journal on Numerical Analysis **10** (1973), no. 2, 413–432.
14. F.W. Grover, *Inductance Calculations: Working Formulas and Tables*, Dover, New York, U.S.A., 1962.
15. R. Ho, K.W. Mai, and M.A. Horowitz, *The future of wires*, Proceedings of the IEEE **89** (2001), no. 4, 490–504.
16. Xin Hu, *Full Wave Analysis of Large Conductor Systems Over Substrates*, Ph.D. thesis, MIT, Cambridge, MA, 2006.
17. J.D. Jackson, *Classical Electrodynamics*, Wiley, New York, U.S.A., 1975.
18. M. Kamon, M.J. Tsuk, and J.K. White, *FastHenry: A multi-pole accelerated 3-D inductance extraction program*, IEEE Transactions on Microwave Theory and Techniques **42** (1994), no. 9, 1750–1758.
19. F. Ling and J.-M. Jin, *Discrete complex image method for Green's functions of general multilayered media*, IEEE Microwave and Guided Wave Letters **10** (2000), no. 10, 400–402.
20. K. Nabors and J. White, *FastCap: A multipole accelerated 3-D capacitance extraction program*, IEEE Transactions on Computer-Aided Design of Integrated Circuits and Systems **10** (1991), no. 11, 1447–1459.
21. S. Ortiz, , Ph.D. thesis, Universite Joseph Fourier, Grenoble, France, 2007.

22. A.E. Ruehli, *Inductance calculations in a complex integrated circuit environment*, IBM Journal of Research and Development **16** (1972), no. 5, 470–481.
23. N. Srivastava, R. Suaya, and K. Banerjee, *Efficient 3D high-frequency impedance extraction for general interconnects and inductors above a layered substrate*, Design Automation and Test in Europe (DATE), 2010 (in press).
24. N. Srivastava, R. Suaya, and K. Banerjee, *High-frequency mutual impedance extraction of VLSI interconnects in the presence of a multi-layer conducting substrate*, Design Automation and Test in Europe (DATE), 2008, 426–431.
25. N. Srivastava, R. Suaya, and K. Banerjee, *Analytical expressions for high-frequency VLSI interconnect impedance extraction in the presence of a multilayer conductive substrate*, IEEE Transactions on Computer-Aided Design of Integrated Circuits and Systems **28** (2009), no. 7, 1047–1060.
26. M.E. Yavuz, M.I. Aksun, and G. Dural, *Critical study of the problems in discrete complex image method*, IEEE International Symposium on Electromagnetic Compatibility, 2003, 1281–1284.
27. M. Yuan, T.K. Sarkar, and M. Salazar-Palma, *A direct discrete complex image method from the closed-form Green's functions in multilayered media*, IEEE Transactions on Microwave Theory and Techniques **54** (2006), no. 3, 1025–1032.